GDCh

Research Articles

Angewandte
Chemie
International Edition
www.angewandte.org

Electrochemical CO2 reduction

Concentrated Formic Acid from CO2 Electrolysis for Directly Driving Fuel Cell

Chao Zhang+, Xiaobin Hao+, Jiatang Wang, Xiayu Ding, Yuan Zhong, Yawen Jiang, Ming-Chung Wu, Ran Long, Wanbing Gong, Changhao Liang, Weiwei Cai,* Jingxiang Low,* and Yujie Xiong*

Abstract: The production of formic acid via electrochemical CO2 reduction may serve as a key link for the carbon cycle in the formic acid economy, yet its practical feasibility is largely limited by the quantity and concentration of the product. Here we demonstrate continuous electrochemical CO2 reduction for formic acid production at 2 M at an industrial-level current densities (i.e., 200 mA cm^{-2}) for 300 h on membrane electrode assembly using scalable lattice-distorted bismuth catalysts. The optimized catalysts also enable a Faradaic efficiency for formate of 94.2 % and a highest partial formate current density of 1.16 A cm^{-2}, reaching a production rate of 21.7 mmol cm^{-2} h^{-1}. To assess the practicality of this system, we perform a comprehensive techno-economic analysis and life cycle assessment, showing that our approach can potentially substitute conventional methyl formate hydrolysis for industrial formic acid production. Furthermore, the resultant formic acid serves as direct fuel for air-breathing formic acid fuel cells, boasting a power density of 55 mW cm^{-2} and an exceptional thermal efficiency of 20.1 %.

Introduction

The overwhelming emission of anthropogenic CO2 into the atmosphere due to the growing dependence of human society on fossil fuels has ignited immense global environ-mental problems. Therefore, there is a pressing demand for the mitigation of CO2 concentration by a paradigm shift of energy medium from fossil fuels to green and renewable fuels.[1,2] In light of this desire, electrochemical CO2 reduction reaction (ECO2RR) powered by renewable electricity for fuel production, which can act as a substitute energy medium or supplement for the current fossil fuel economy, has aroused wide attention.[3,4] If such a strategy can be realized, it can not only relieve us from the high dependency on fossil fuels, but also close the carbon cycle toward achieving carbon neutrality. With respect to the gaseous ECO2RR products, the liquid ECO2RR products are more prominent and ready to be used as the energy medium due to their relatively high energy density, easy storage and transport, and also high compatibility with the current fossil fuel infrastructures.[5,6] Among various potential liquid products, formic acid (FA) shows great potential because it has recently reached a commercially relevant current density via ECO2RR (see also Figure S1).[7,8] Furthermore, the concept of FA economy has been recently coined to employ FA from ECO2RR (Figure S2) as an energy vector within the global economy, igniting gigantic attention from both the general public and the scientific community.[9,10]

Despite notable achievements in ECO2RR for FA production, there remain significant challenges in achieving the requisite activity, selectivity and stability for the continuous and efficient production of FA, limiting the industrial applications.[11,12] Bismuth (Bi) catalysts, attributed to their lower energy barrier to form *CO2^{-} intermediates which can readily protonate to yield formate, have demonstrated substantial potential for advancing ECO2RR in FA production.[13–15] For instance, Yang et al. recently showed that the bromide-activated Bi catalysts owned excellent

[*] C. Zhang,+ X. Hao,+ X. Ding, Y. Zhong, Y. Jiang, Prof. R. Long,
W. Gong, J. Low, Prof. Y. Xiong
Hefei National Research Center for Physical Sciences at the
Microscale, School of Chemistry and Materials Science, and
National Synchrotron Radiation Laboratory, University of Science
and Technology of China; Hefei, Anhui, 230026, China
E-mail: jxlow@ustc.edu.cn
        yjxiong@ustc.edu.cn

C. Zhang,+ Prof. Y. Xiong
Suzhou Institute for Advanced Research, University of Science and
Technology of China, Suzhou, Jiangsu, 215123, China

J. Wang, Prof. W. Cai
Sustainable Energy Laboratory, Faculty of Materials Science and
Chemistry, China University of Geosciences Wuhan,
388 Lumo Road, Wuhan, Hubei, 430074, China
E-mail: caiww@cug.edu.cn

M.-C. Wu
Department of Chemical and Materials Engineering,
Chang Gung University, Taoyuan, 33302 Taiwan

C. Liang
Key Laboratory of Materials Physics, Institute of Solid State Physics,
HFIPS, Chinese Academy of Sciences, Hefei, Anhui, 230031, China

Prof. Y. Xiong
Anhui Engineering Research Center of Carbon Neutrality, The Key
Laboratory of Functional Molecular Solids, Ministry of Education,
Anhui Laboratory of Molecular-Based Materials, College of
Chemistry and Materials Science, Anhui Normal University,
Wuhu, Anhui, 241002, China

[+] These authors contributed equally to this work.

performance, achieving a high current density of 148 mA cm^{-2} and HCOOH selectivity of 91 %.[16] Nevertheless, the reported Bi-based catalysts are often plagued by complex and small-scale production methods, along with poor stability.[17–19] Moreover, it is important to stress here that the FA produced from ECO$_2$RR usually in the form of formate owes to the use of conventional electrolytes (e.g., KHCO$_3$ and KOH) in H-type cells or flow cells, leading to a high cost of purification.[20–22] Some attempts have been made to employ solid electrolyte reactor for substituting the conventional system, realizing the continuous production of 0.1 M formic acid solution for 180 h,[23] yet the achieved FA concentration remains relatively low.[24–27] For these reasons, the exploration of the ECO$_2$RR system with efficient Bi-based catalysts and advanced system setup to directly transform CO$_2$ into concentrated FA with high selectivity and stability over large current density is highly desirable.

Lattice distortion defects can have a critical influence on the structural heterogeneities and surface electronic properties of catalysts without interfering with their chemical composition, and can bring tangible benefits for facilitating catalytic reactions.[28–31] Herein, we demonstrate the superior ECO$_2$RR performance over Bi-based catalysts with rich lattice distortion defects (RD-Bi) to produce FA in large quantities and high concentrations, which can be directly employed for driving the direct FA fuel cell (DFAFC). Specifically, we employ the laser-irradiation in liquid-phase (LIL) method to prepare amorphous BiO$_x$ nanoparticles (NPs) in a scalable manner, which can be facilely electro-reduced to RD-Bi. The resultant RD-Bi can be used as a cathode catalyst in a solid electrolyte reactor with our developed moist heat ventilation collection system, allowing it to continuously produce FA solution in large quantities with a concentration of 2 M. In situ diffuse reflectance-infrared Fourier-transform spectroscopy (DRIFTS) measurements and theoretical calculations demonstrate that the existence of lattice distortion is beneficial to the binding of *OCHO intermediates on the catalysts and gives rise to an outstanding activity and selectivity of FA from ECO$_2$RR. Additionally, we perform the comprehensive techno-economic analysis (TEA) and life cycle assessment (LCA) for our ECO$_2$RR system and conventional methyl formate hydrolysis system, which validate not only the economic viability but also the environmental conscientiousness of our proposed technology, positioning it as a front-running solution in the realm of FA production. To further demonstrate the practicability of the system, we directly utilize the produced FA for powering up the air-breathing DFAFC without purification, giving a power density of 55 mW cm^{-2} and reaching an overall (i.e., starting from storing electricity in chemicals to discharging the electricity from chemicals) efficiency of up to 20.1 %, which is comparable with the thermal efficiency of the gasoline engine.

Results and Discussion

We first prepare the amorphous BiO$_x$ (denoted as BiO$_x$-LIL), which can be easily stored and transformed into metallic Bi through electroreduction upon use, via the LIL method using Bi powder as the precursors (Figure 1a). As shown in Figure 1b, the size of prepared BiO$_x$-LIL (ca. 50 nm) is substantially smaller than that of bulk Bi (Figure S3), suggesting the crushing of bulk Bi during the LIL process. Interestingly, no evident lattice fringes and diffractions can be observed in the HRTEM image and the corresponding fast Fourier transform (FFT) pattern and XRD pattern of BiO$_x$-LIL also demonstrate its amorphous structure (Figure 1c, Figure S4 and S5). Upon electroreduction, these defects can be preserved during the rapid transformation of BiO$_x$-LIL to metallic Bi, which can be beneficial for catalytic application. According to X-ray photoelectron spectroscopy (XPS) characterizations shown in Figure S6, BiO$_x$-LIL demonstrates a higher ratio of oxygen vacancies than Bi$_2$O$_3$ (prepared by calcination of bulk Bi), which can be also corroborated by electron spin resonance (ESR) spectra (Figure S7).[32,33] Based on X-ray absorption spectroscopy characterizations (Figure S8, S9 and Table S2), the Bi–O bond length (R) and coordination number (CN) of BiO$_x$-LIL can be determined to be 2.06 Å and 3.2, respectively. These R and CN values are obviously smaller than those of Bi$_2$O$_3$ (R=2.11 Å, CN=5.0), indicating the unsaturated coordination environment of BiO$_x$-LIL with contractive Bi–O bonds due to the amorphous structure. According to the above characterization, we can affirm that the LIL method can be a simple and effective
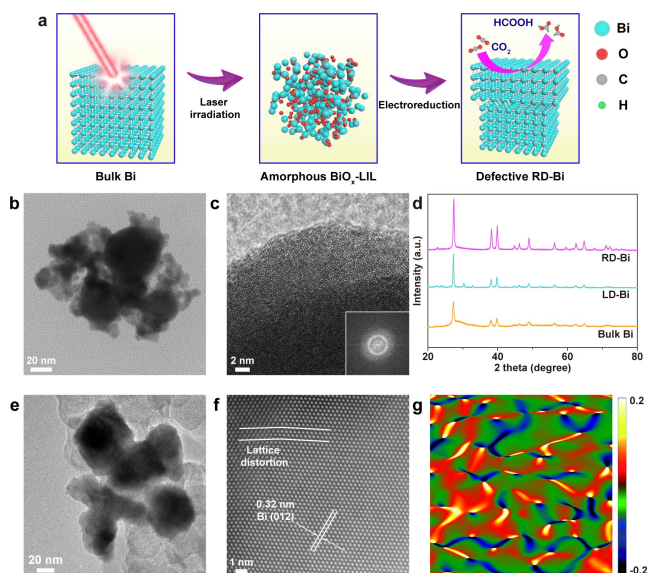

Figure 1. (a) Schematic illustration for the preparation procedure of RD-Bi. (b and c) TEM (b) and HRTEM (c) images of BiO$_x$-LIL. The inset of (c) shows the FFT pattern. (d) XRD patterns of bulk Bi, RD-Bi and LD-Bi. (e and f) TEM (e) and HAADF-STEM (f) images of RD-Bi. (g) Strain distributions of ε$_{xx}$ processed via GPA for RD-Bi. Compressive strain is denoted by the colour from green to dark blue, while tensile strain is denoted by the colour from red to bright yellow.

method for the preparation of amorphous materials (Figure S10). Specifically, BiO_x-LIL possesses an amorphous structure with abundant unsaturated sites, which allows it to be an ideal precursor for the preparation of defective metallic Bi catalysts for ECO_2RR.

The RD-Bi is obtained from amorphous BiO_x-LIL by in situ electrochemical conversion method. As shown in Figure 1d and Figure S11, the XRD pattern of RD-Bi displays high crystallinity and can be indexed to rhombohedral Bi (PDF# 85-1331), and its peaks shift toward a higher angle direction compared to bulk Bi and Bi samples with fewer defects converted from Bi_2O_3 (LD-Bi), revealing the smaller interplanar spacing of RD-Bi. These results imply the existence of compressive strain in RD-Bi attributed to the lattice distortions in its structure, which can be also supported by the in situ Raman spectroscopy (Figure S12 and S13).[34,35] Furthermore, as revealed by the transmission electron microscopy (TEM) image (Figure 1e), the RD-Bi presents a spherical morphology with a mean diameter of 50 nm mixed with carbon black. The high-angle annular dark-field-scanning TEM (HAADF-STEM) image shows that the lattice spacing of RD-Bi is ca. 0.32 nm (Figure 1f), which is attributed to the rhombohedral Bi (012) plane. Abundant lattice distortion can be clearly observed on RD-Bi (Figure 1f), further confirming its defect-rich features. Moreover, geometric phase analysis (GPA) is performed to

investigate the lattice strain distribution of RD-Bi (Figure 1g),[36] manifesting that the main strain in RD-Bi NPs is the compressive strain (see also Figure S14). The chemical status of the RD-Bi is revealed by XPS spectra (Figure S15), indicating the formation of metallic Bi in RD-Bi.[37,38]

We then evaluate the ECO_2RR performance of all the prepared samples in argon- (Ar-) or CO_2-saturated 0.5 M $KHCO_3$ using an H-type cell. As shown in Figure S16, the linear sweep voltammetry (LSV) curves of all the prepared samples show the enhancement of current density in CO_2-saturated electrolyte compared to that in Ar-saturated electrolyte, indicating the high selectivity of these Bi-based electrocatalysts toward ECO_2RR. Moreover, the LSV curves shown in Figure 2a reveal that RD-Bi possesses the largest current density among all the prepared electrocatalysts. Furthermore, formate is the main product of ECO_2RR for RD-Bi in the whole potential range (Figure 2b), and a minor amount of H_2 and CO can be detected (Figure S17). Specifically, the Faradaic efficiency (FE) of formate for RD-Bi retains over 80 % in a wide potential range from −0.7 to −1.2 V versus RHE. In contrast, bulk Bi and LD-Bi display the FE of formate below 80 % in the whole potential range. As shown in Figure 2c, the $j_{formate}$ of RD-Bi is dramatically higher than that of bulk Bi and LD-Bi in the whole potential range, reaching the highest $j_{formate}$ of 44.1 mA cm^{-2}, which corresponds to a formate production rate of 823.5 μmol h^{-1}
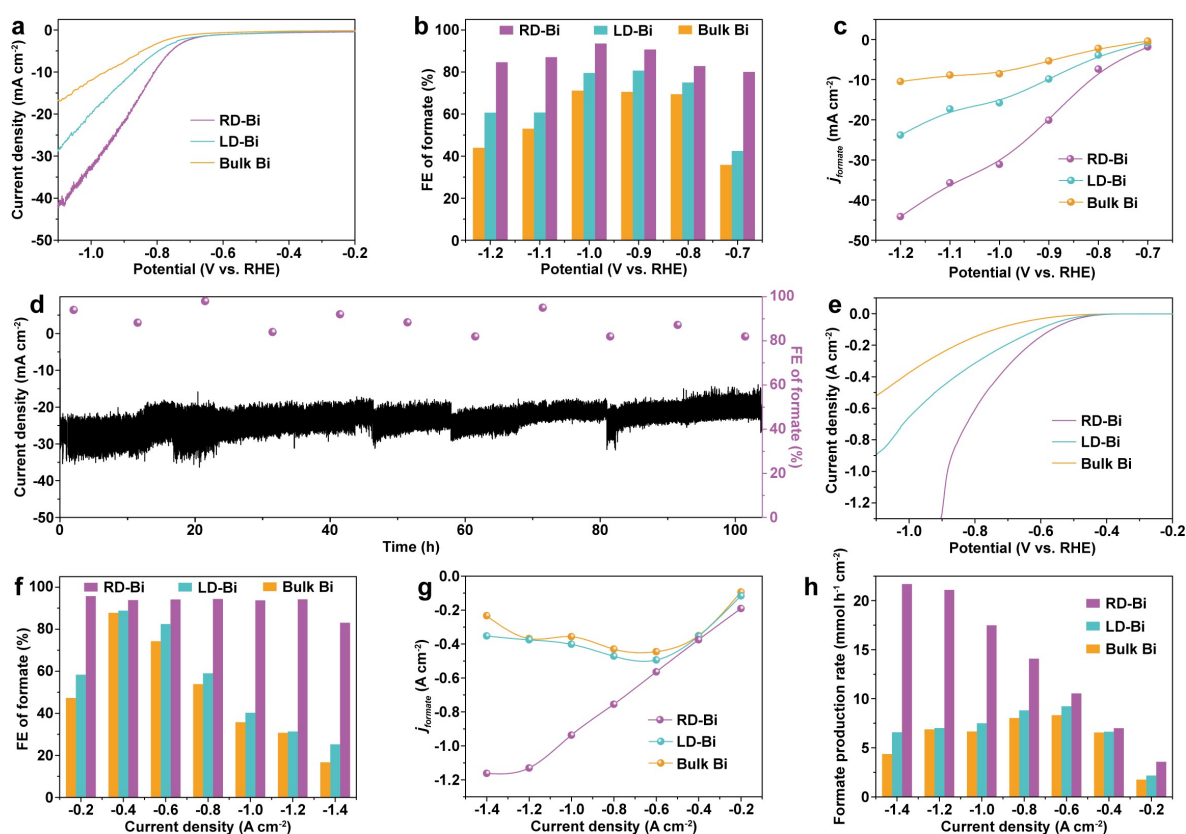
Figure 2. (a) LSV curves, (b) FEs of formate at different applied potentials and (c) partial current density of formate for RD-Bi, bulk Bi and LD-Bi measured in CO_2-saturated 0.5 M $KHCO_3$ electrolyte in an H-type cell. (d) Long-term ECO_2RR test of RD-Bi for 100 h in CO_2-saturated 0.5 M $KHCO_3$ electrolyte at −1 V versus RHE in an H-type cell. (e) LSV curves, (f) FEs of formate at different applied potentials, (g) partial current density of formate and (h) Formate production rates at different current densities for RD-Bi, bulk Bi and LD-Bi measured in flow cell.

Angew. Chem. Int. Ed. **2024**, e202317628 (3 of 8)

© 2024 Wiley-VCH GmbH

cm^{-2} (Figure S18a). This $j_{formate}$ of RD-Bi is 4.2 and 1.9 times higher than that of LD-Bi (23.8 mA cm^{-2}) and bulk Bi (10.5 mA cm^{-2}), respectively. The EE of RD-Bi surpasses 50 % in the whole studied potential range and a maximum value of 63 % is achieved at -0.9 V versus RHE (Figure S18b), which is far higher than the maximum values of bulk Bi (50.6 %) and LD-Bi (56 %). In addition, the activity and selectivity of RD-Bi exceed most reported electrocatalysts for ECO$_2$RR toward FA production (Figure S19). Such a superior ECO$_2$RR performance can be also reproduced using the commercial Bi powder as a precursor for BiO$_x$-LIL, further confirming the practicability of our developed lattice-distorted catalysts (Figure S20). Moreover, the RD-Bi presents high stability (Figure 2d), which delivers a negligible current density decay and a mean FE for formate around 90 % for 100 h continuous electrocatalytic test. Moreover, the TEM images indicate that the structure and morphology of RD-Bi are well maintained after the stability test (Figure S21), further demonstrating the high stability of RD-Bi.

Considering the CO$_2$ mass transport limitation in the conventional H-type cells, the system can hardly reach a high current density. To this end, the flow cell, which can facilitate the diffusion of CO$_2$ to the surface of catalysts, is set up to further investigate the ECO$_2$RR performance of RD-Bi (Figure S22). As shown in Figure 2e, the LSV curve of RD-Bi displays a large current density of 1.3 A cm^{-2} at -0.91 V using a flow cell reactor, which is significantly higher than that of bulk Bi and LD-Bi. Subsequently, chronopotentiometry tests are performed between 0.2 and 1.4 A cm^{-2} to investigate the product of ECO$_2$RR over all the prepared samples. RD-Bi displays a high FE of formate of 94.2 % at 1.2 A cm^{-2} and achieves high FE of formate over 90 % in a wide applied current density range from 0.2 to 1.2 A cm^{-2} (Figure 2f and Figure S23). With this FE of formate, RD-Bi also achieves the highest $j_{formate}$ of 1.16 A cm^{-2} among all the prepared samples (Figure 2g), corresponding to the formate production rate of 21.7 mmol cm^{-2} h^{-1}, which is one of the highest values among the recently reported ECO$_2$RR (Figure 2h and S24). In contrast, the FE of formate for both bulk Bi and LD-Bi electrocatalysts are <90 % and only reach the $j_{formate}$ lower than 0.5 A cm^{-2}.

Despite the high current density achieved in the flow cell for RD-Bi, formate is formed as the main product, requiring further purification to obtain formic acid. In addition, the poor stability of the flow cell also limits its FA production in large quantities (>100 mL) with high concentrations (>1 M) (Figure S25 and S26). Thus, an MEA electrolyzer, which contains a proton-conducting solid-state electrolyte to avoid the generation of formate, is employed (Figure 3a and Figure S27 and S28). Furthermore, we have set up a moist heat ventilation collection system (see Materials and Methods section, Figure S29) to collect FA produced from the ECO$_2$RR, allowing the tunable concentration of the FA by simply changing the humidity of the system. Excitingly, the current density of our device can reach over 200 mA cm^{-2} at a cell potential of 4.1 V and deliver a peak FE for FA of 86.5 % at 150 mA cm^{-2} (Figure 3b and c),

which is comparable to the recently reported catalysts (Figure S30 and Table S3). More importantly, our system realizes the continuous production of 2 M FA solutions at an operating current density of 200 mA cm^{-2} for 300 h without significant performance deterioration (Figure 3d, Figure S31 and Movie S1), which has never been achieved by previous research (Table S4). The single-pass CO$_2$ conversion is determined to be ca. 17.3 % (Figure S32). As such, 1 L of FA with a concentration of 2 M is successfully prepared using only 4 mg of catalysts. In contrast, the FA concentration is only 0.2 M if we use deionized water at a flow rate of 0.5 mL min^{-1} to release the HCOOH solution (Figure S33). More importantly, such a system can also work by substituting the electrochemical station with the solar cell as a power supply, and continuously produce pure FA solution in large quantities with high concentrations (Figure S34), verifying the possibility of the system being driven by renewable solar energy and its high potential for off-grid applications. Such a production of FA solution with high concentration can provide a prospect of the commercialization of ECO$_2$RR (Figure S35 and Table S5).

To attest to the superiority of the RD-Bi in ECO$_2$RR, we calculate the electrochemical surface area (ECSA) of the prepared Bi-based catalysts by measuring their double-layer capacitance (C_{dl}). As shown in Figure S36, the C_{dl} of RD-Bi is 1.12 mF cm^{-2}, corresponding to the ECSA of 56 cm^2, which is higher than that of bulk Bi ($C_{dl}=0.65$ mF cm^{-2}, ECSA = 32.5 cm^2) and LD-Bi ($C_{dl}=0.75$ mF cm^{-2}, ECSA = 37.5 cm^2). In addition, ECSA-normalized $j_{formate}$ of RD-Bi (-0.79 mA cm^{-2}) is merely 2.47 and 1.23 times higher than that of bulk Bi (-0.32 mA cm^{-2}) and LD-Bi (-0.64 mA cm^{-2}) at -1.2 V versus RHE (Figure S37), respectively, indicating that the increase in the number of surface active sites is not the only reason for the superior activity of the RD-Bi. Subsequently, the Tafel slopes in Figure S38a show that RD-Bi displays the smallest Tafel slope of 166 mV dec^{-1} among all the prepared samples, implying its fastest reaction kinetics for ECO$_2$RR attributed to its abundant lattice distortion. Electrochemical impedance spectroscopy (EIS) measurements indicate that the arc diameter in the Nyquist plot of RD-Bi is smaller than that of bulk Bi and LD-Bi (Figure S38b), suggesting its smaller charge transfer resistance and faster electron transfer. Such rapid electron transfers of RD-Bi allow the adsorbed CO$_2$ molecules to be efficiently converted into intermediates or final products, leading to an accelerated kinetics process.

Furthermore, OH$^-$ is employed as a substitute to evaluate the binding affinity of *CO$_2^-$ intermediates over the catalysts by measuring the oxidative LSV in an Ar-saturated KOH electrolyte.[39,40] As shown in Figure S38c, RD-Bi displays the lowest overpotential of OH$^-$ adsorption among all the studied samples, suggesting its strongest binding of OH$^-$. Such a superior OH$^-$ binding on RD-Bi manifests its capability of efficiently stabilizing *CO$_2^-$ intermediates and reducing the energy barrier for HCOOH formation. Additionally, in situ diffuse reflectance infrared Fourier transform spectroscopy (DRIFTS) is conducted to further explore the reactant intermediates formed during
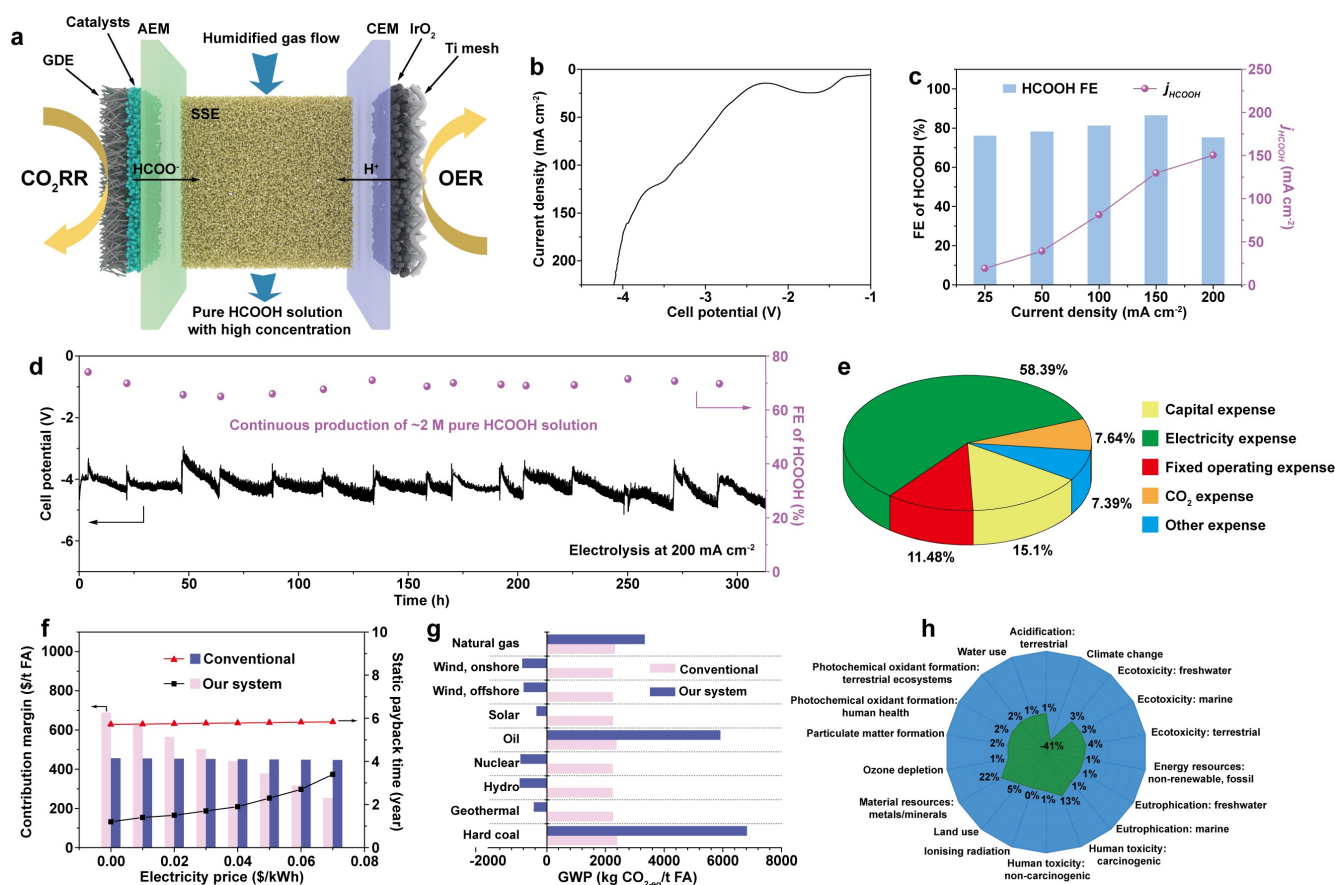
Figure 3. (a) Schematic illustration of the ECO₂RR in MEA with SSE to produce pure HCOOH solution with high concentration. (b and c) LSV curve (b) and FE of HCOOH at different cell current densities and the corresponding partial current densities of HCOOH for RD-Bi catalyst in MEA with SSE (c). (d) Long-term stability test and the corresponding FEs of CO_2 reduction to FA solution at 200 mA cm⁻² over RD-Bi catalyst in MEA with SSE. (e) Subdivided cost of ECO₂RR method to produce 1 t FA. (f) Comparison of contribution margin and static payback time of our ECO₂RR and conventional methyl formate hydrolysis methods for the production of FA with different electricity prices. (g) Global warming potential of our ECO₂RR and conventional methyl formate hydrolysis methods for the production of FA using different electricity sources. (h) Comparison of the environmental impact indicator results (normalized to the largest value of each indicator) for the conventional methyl formate hydrolysis and our system to produce FA powered by hydroelectricity.

the ECO₂RR process. As shown in Figure S39, the peak located around 1,380 cm⁻¹ corresponds to the vibration of O–C–O in *OCHO,[41,42] which is the key intermediate for the formation of formate. The intensity of the peak for *OCHO over RD-Bi is promoted at a more negative potential (Figure S39a). Notably, the intensities of the peak for *OCHO over LD-Bi and bulk Bi are substantially weaker compared to RD-Bi (Figure S39b,c). This can be the main reason for the high efficiency and selectivity of the RD-Bi toward FA production. Moreover, another peak centred at 2,360 cm⁻¹ assigned to OCO asymmetrical stretching ($v_{as}(CO_2)$) can be also found,[43,44] indicating the adsorption of CO_2 on RD-Bi. Interestingly, the peak intensity of $v_{as}(CO_2)$ peak for RD-Bi is enhanced with the decreasing applied potential from −0.3 to −0.8 V, and then gradually decays with the further decreasing applied potential from −0.8 to −1.3 V (Figure S39d). This observation is an outcome of the transformation of the absorbed CO_2 into *OCHO intermediates at a sufficiently negative applied potential (see also Figure S39e,f). Our results, supported by

the in situ characterizations, reveal a regime, where the CO_2 adsorption and formation of the *OCHO intermediate become prevalent on the RD-Bi. This finding serves as a cornerstone in establishing the fundamental underpinnings of the extraordinary FA production performance in this work.

To understand the underlying roles of the lattice distortion in enhancing the ECO₂RR of the RD-Bi, we perform the density functional theory (DFT) calculations. Based on the experimental characterization, the perfect (representing Bi, Figure S40a) and lattice distorted (representing RD-Bi, Figure S40b) Bi (012) surfaces are built. It is discovered that the Bi–Bi bonds are shortened from 3.10 Å in the Bi to 2.92 Å in the RD-Bi, which is in good accordance with the structural characterization results. Moreover, the potential energies of CO_2 conversion to FA on Bi and RD-Bi are investigated based on the configurations shown in Figure S41 and S42. The potential energy on the surface with lattice distortion is lower than that on the perfect surface (Figure S43a), suggesting higher forma-

tion activity of the formate on the surface with lattice distortion. Notably, the adsorption energy of *OCHO on the RD-Bi (−1.75 eV) is substantially lower than that on theBi (−0.56 eV), implying that the key intermediates can be easily stabilized on the surface with lattice distortion (Figure S43b). According to the partial density of states (PDOS) of Bi (012) with and without lattice distortion (Figure S43c,d), both of their PDOS diagrams show the overlap between Bi 6 s and O 2p orbital, which can contribute to the major interaction of *OCHO with Bi surface. More importantly, the energy level for the interaction between O 2p and Bi 6 s orbital on the surface with lattice distortion is significantly lower than that on the perfect surface, further manifesting the strong interaction between the Bi and the adsorbed *OCHO to allow the subsequent formation of the FA.

The practical applications of such a technology hinge upon its economic and environmental feasibility. Therefore, we conduct TEA and LCA to compare the FA production from our ECO_2RR system with the conventional methyl formate hydrolysis system (see Methods section and Table S6–S24 for calculation details). Our findings reveal that our system exhibits several advantages over the conventional methods (Figure 3e,f and Figure S44–S48). It demonstrates lower capital expenses and shorter static payback time. It is noteworthy that electricity prices play a dominant role in the overall production costs, accounting for approximately 60 % of the total expenses (Figure 3e and Table S25–S31). Recognizing the significance of electricity prices, we perform a sensitivity analysis to understand their impact on our system's contribution margin and static payback time (Figure 3f and Table S32). The results indicate that our system is highly sensitive to electricity prices, with the contribution margin increasing and the static payback time increasing as electricity prices rise. Interestingly, the contribution margin of our system is higher than that of the conventional method when electricity prices are below 0.03 $/kWh. Despite this, the static payback time of our system consistently remains shorter than the conventional method, highlighting the economic superiority of our system for FA production. Regarding the LCA, our system significantly outperforms the conventional method by using renewable energy as an electricity source (Figure 3g), showing high potential in reducing carbon emission (e.g., −353.6 kg CO_{2-eq}/t FA using electricity from solar energy and −926.6 kg CO_{2-eq}/t FA using hydroelectricity, see Figure S49 and Table S12). Furthermore, when comparing the environmental impacts of ECO_2RR powered by hydroelectricity with the conventional methyl formate hydrolysis, we find that the electrochemical process displays much lower impacts on 18 environmental issues (Figure 3h). The above results demonstrate that our system is not only an economically superior choice but also an environmentally friendly technology compared to the conventional method for FA production.

The ultimate aim of this work is to demonstrate the feasibility and practicability of the ECO_2RR for substituting conventional methyl formate hydrolysis in ECO_2RR. To further demonstrate the superiority of the system, we

directly employ the produced FA for driving the direct FA fuel cell (DFAFC). To preserve the non-corrosive and low toxicity features of FA (Table 35) and guarantee sufficient energy output from the DFAFC, the moderate concentration (2 M) of FA is the target, and has been successfully produced in large quantity from our developed ECO_2RR system. Then, a passive air-breathing DFAFC containing 40 wt % (wt %) PdPt/C as anode catalyst and 20 wt % Pt/C as cathode catalyst is assembled (Figure 4a and Figure S50). As shown in Figure 4b, the FA solution produced from ECO_2RR can not only drive the air-breathing DFAFC, but also yield a power density of up to 55 mW cm^{-2} at 25 °C and ambient pressure, confirming the practicability of the produced FA from our developed system. Moreover, the galvanostatic discharge curve in Figure 4c presents that the voltage of DFAFC is about 0.55 V at the discharge current density of 50 mA cm^{-2} and no obvious voltage drop is observed in 2 h, demonstrating the outstanding durability of air-breathing DFAFC driven by 2 M FA produced from ECO_2RR. Excitingly, such high discharge power density and stability of the DFAFC driven by the FA produced from our ECO_2RR system can be employed for powering up the light-emitting diode (Figure 4d) and a small-scale car system (Figure 4e and Movie S2). More interestingly, the thermal efficiency of the DFAFC is ca. 45.4 % based on the galvanostatic discharge curve. In other words, the overall thermal efficiency of our developed system, starting from storing electricity in chemicals (i.e., conversion of CO_2 to FA) to discharging the electricity from chemicals (i.e.,
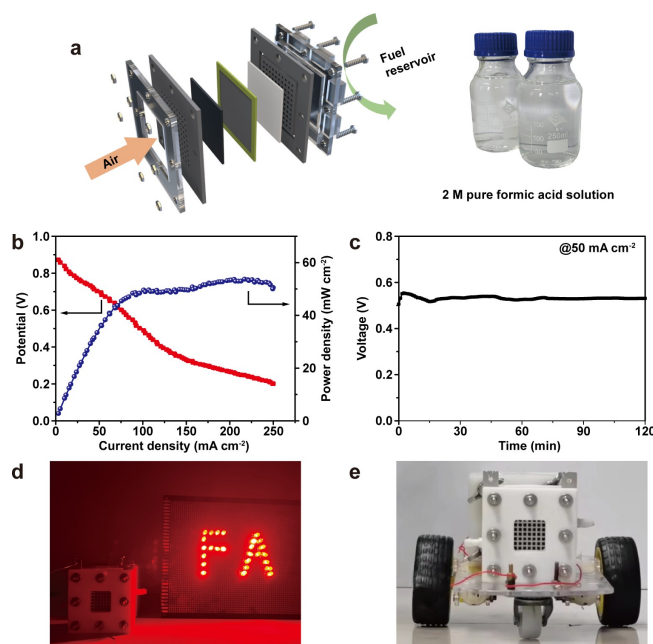
Figure 4. (a) Schematic illustration of air-breathing DFAFC and photograph of 2 M formic acid solution produced from our developed ECO_2RR system. (b and c) Power density plot and discharge curve (b) and galvanostatic discharge curves (c) at a current density of 50 mA cm^{-2} for DFAFC by directly using the FA produced from ECO_2RR as fuels. (d and e) Photographs of the light-emitting diode (d) and small-scale car system (e) powered by the air-breathing DFAFC.

conversion of FA to CO_2), can reach 12.4–20.1 % (Table S36), which is very close to the thermal efficiency of the conventional gasoline engine (i.e., 20–40 %). This satisfactory energy efficiency of CO_2 to formic acid and then to electricity the conversion recognized as the key link paves the way to a complete loop in the formic acid economy.

Conclusion

This study developed a LIL method for the scalable preparation of Bi-based catalysts for efficient and selective ECO_2RR toward FA production. Such a catalyst delivers a high Faradaic efficiency for formate of 94.2 % at 1.2 A cm^{-2} and reaches a formate production rate of 21.7 mmol h^{-1} cm^{-2}. We also realize the continuous production of pure FA solution with a high concentration of 2 M at 200 mA cm^{-2} for 300 h by using MEA containing SSE equipped with a moist heat ventilation collection system. More importantly, we can directly employ the produced FA to drive air-breathing DFAFC, achieving a power density of 55 mW cm^{-2} and an overall efficiency of 20.1 %, closing the carbon cycle loop of the formic acid economy. This work demonstrates the feasibility of the formic acid economy to substitute the fossil fuel economy as the energy vector in human society.

Acknowledgements

Conflict of Interest

The authors declare no conflict of interest.

Data Availability Statement

The data that support the findings of this study are available from the corresponding author upon reasonable request.

[1] H. Rao, L. C. S. Chmidt, J. Bonin, M. Robert, *Nature* **2017**, *548*, 74–77.

[2] C. T. Dinh, T. Burdyny, M. G. Kibria, A. Seifitokaldani, C. M. Gabardo, P. Arquer, A. Kiani, J. P. Edwards, P. Luna, O. S. Bushuyev, C. Zou, R. Q. Bermudez, Y. Pang, D. Sinton, E. H. Sargent, *Science* **2018**, *360*, 783–787.

[3] D. F. Gao, R. M. Aran-Ais, H. S. Jeon, B. R. Cuenya, *Nat. Catal.* **2019**, *2*, 198–210.

[4] X. Y. Tan, C. Yu, Y. Ren, S. Cui, W. Li, J. Qiu, *Energy Environ. Sci.* **2021**, *14*, 765–780.

[5] P. Zhu, H. T. Wang, *Nat. Catal.* **2021**, *4*, 943–951.

[6] Y. Y. Birdja, E. Pérez-Gallent, M. C. Figueiredo, A. J. Göttle, F. Calle-Vallejo, M. T. M. Koper, *Nat. Energy* **2019**, *4*, 732–745.

[7] Q. Gong, P. Ding, M. Xu, X. Zhu, M. Wang, J. Deng, Q. Ma, N. Han, Y. Zhu, J. Lu, Z. Feng, Y. Li, W. Zhou, Y. Li, *Nat. Commun.* **2019**, *10*, 2807.

[8] M. Zhang, W. Wei, S. Zhou, D. Ma, A. Cao, X. Wu, Q. Zhu, *Energy Environ. Sci.* **2021**, *14*, 4998–5008.

[9] S. Chatterjee, I. Dutta, Y. Lum, Z. P. Lai, K. W. Huang, *Energy Environ. Sci.* **2021**, *14*, 1194–1246.

[10] I. Dutta, S. Chatterjee, H. Cheng, R. K. Parsapur, Z. Liu, Z. Li, E. Ye, H. Kawanami, J. S. C. Low, Z. Lai, X. J. Loh, K. Huang, *Adv. Energy Mater.* **2022**, *12*, 2103799.

[11] K. Fernández-Caso, G. Díaz-Sainz, M. Alvarez-Guerra, A. Irabien, *ACS Energy Lett.* **2023**, *8*, 1992–2024.

[12] S. Liu, C. Wang, J. Wu, B. Tian, Y. Sun, Y. Lv, Z. Mu, Y. Sun, X. Li, F. Wang, Y. Wang, L. Tang, P. Wang, Y. Li, M. Ding, *ACS Catal.* **2021**, *11*, 12476–12484.

[13] X. Liang, Q. Zheng, N. Wei, Y. Lou, S. Hu, K. Zhao, H. Liao, N. Tian, Z. Zhou, S. Sun, *Nano Energy* **2023**, *114*, 108638.

[14] L. Lv, R. Lu, J. Zhu, R. Yu, W. Zhang, E. Cui, X. Chen, Y. Dai, L. Cui, J. Li, L. Zhou, W. Chen, Z. Wang, L. Mai, *Angew. Chem. Int. Ed.* **2023**, *135*, e202303.

[15] J. Zhu, J. Li, R. Lu, R. Yu, S. Zhao, C. Li, L. Lv, L. Xia, X. Chen, W. Cai, J. Meng, W. Zhang, X. Pan, X. Hong, Y. Dai, Y. Mao, J. Li, L. Zhou, G. He, Q. Pang, Y. Zhao, C. Xia, Z. Wang, L. Dai, L. Mai, *Nat. Commun.* **2023**, *14*, 4670.

[16] S. Yang, H. An, S. Arnouts, H. Wang, X. Yu, J. Ruiter, S. Bals, T. Altantzis, B. M. Weckhuysen, W. Stam, *Nat. Catal.* **2023**, *6*, 796–806.

[17] H. Shen, Y. Zhao, L. Zhang, Y. He, S. Yang, T. Wang, Y. Cao, Y. Guo, Q. Zhang, H. Zhang, *Adv. Energy Mater.* **2023**, *13*, 2202818.

[18] L. Yi, J. Chen, P. Shao, J. Huang, X. Peng, J. Li, G. Wang, C. Zhang, Z. Wen, *Angew. Chem. Int. Ed.* **2020**, *59*, 20112–20119.

[19] F. Yang, A. O. Elnabawy, R. Schimmenti, P. Song, J. Wang, Z. Peng, S. Yao, R. Deng, S. Song, Y. Lin, M. Mavrikakis, W. Xu, *Nat. Commun.* **2020**, *11*, 1088.

[20] Z. Wang, Y. Zhou, D. Liu, R. Qi, C. Xia, M. Li, B. You, B. Xia, *Angew. Chem. Int. Ed.* **2022**, *61*, e202200552.

[21] D. M. Weekes, D. A. Salvatore, A. Reyes, A. X. Huang, C. P. Berlinguette, *Acc. Chem. Res.* **2018**, *51*, 910–918.

[22] B. Jia, L. Li, C. Xue, J. Kang, L. Liu, T. Guo, Z. Wang, Q. Huang, S. Guo, *Adv. Mater.* **2023**, *35*, 2305587.

[23] T. Zheng, C. Liu, C. Guo, M. Zhang, X. Li, Q. Jiang, W. Xue, H. Li, A. Li, C. W. Pao, J. Xiao, C. Xia, J. Zeng, *Nat. Nanotechnol.* **2021**, *16*, 1386–1393.

[24] C. Xia, P. Zhu, Q. Jiang, Y. Pan, W. Liang, E. Stavitski, H. N. Alshareef, H. Wang, *Nat. Energy* **2019**, *4*, 776–785.

[25] L. Fan, C. Xia, P. Zhu, Y. Lu, H. Wang, *Nat. Commun.* **2020**, *11*, 3633.

[26] B. Jia, Z. Chen, C. Li, Z. Li, X. Zhou, T. Wang, W. Yang, L. Sun, B. Zhang, *J. Am. Chem. Soc.* **2023**, *145*, 14101–14111.

[27] X. Wang, M. Zhou, M. Wang, W. Wang, Z. Yang, Y. Zhang, Q. Li, H. Ning, M. Wu, *Nano Lett.* **2023**, *23*, 10946–10954.

[28] S. Maiti, K. Maiti, M. T. Curnan, K. Kim, K. J. Noh, J. W. Han, *Energy Environ. Sci.* **2021**, *14*, 3717–3756.

[29] D. Yan, Y. Li, J. Huo, R. Chen, L. Dai, S. Wang, *Adv. Mater.* **2017**, *29*, 1606459.

[30] R. Chattot, O. Le Bacq, V. Beermann, S. Kuhl, J. Herranz, S. Henning, L. Kuhn, T. Asset, L. Guetaz, G. Renou, J. Drnec, P. Bordet, A. Pasturel, A. Eychmuller, T. J. Schmidt, P. Strasser, L. Dubau, F. Maillard, *Nat. Mater.* **2018**, *17*, 827–833.

[31] R. G. Mariano, M. Kang, O. J. Wahab, I. J. McPherson, J. A. Rabinowitz, P. R. Unwin, M. W. Kanan, *Nat. Mater.* **2021**, *20*, 1000–1006.

[32] Y. X. Li, M. M. Wen, Y. Wang, G. Tian, C. Y. Wang, J. C. Zhao, *Angew. Chem. Int. Ed.* **2021**, *60*, 910–916.

[33] B. Lei, W. Cui, J. P. Sheng, H. Wang, P. Chen, J. Y. Li, Y. J. Sun, F. Dong, *Sci. Bull.* **2020**, *65*, 467–476.

[34] Z. Q. Wang, X. L. Zu, X. D. Li, L. Li, Y. Wu, S. M. Wang, P. Q. Ling, Y. Zhao, Y. F. Sun, Y. Xie, *Nano Res.* **2022**, *15*, 6999–7007.

[35] X. H. Sun, H. L. Zhao, J. Y. Chen, W. Zhong, B. B. Zhu, L. Tao, *Nanoscale* **2021**, *13*, 2648–2657.

[36] M. J. Hytch, F. Houdellier, *Microelectron. Eng.* **2007**, *84*, 460–463.

[37] F. M. Allioux, S. Merhebi, M. B. Ghasemian, J. B. Tang, A. Merenda, R. Abbasi, M. Mayyas, T. Daeneke, A. P. O'Mullane, R. Daiyan, R. Amal, K. Kalantar-Zadeh, *Nano Lett.* **2020**, *20*, 4403–4409.

[38] H. Zhang, Z. F. Liang, C. Q. Huang, L. Xie, H. B. Wang, J. P. Hu, Z. Jiang, F. Song, *J. Catal.* **2022**, *410*, 1–9.

[39] A. Salehi-Khojin, H. R. M. Jhong, B. A. Rosen, W. Zhu, S. C. Ma, P. J. A. Kenis, R. I. Masel, *J. Phys. Chem. C* **2013**, *117*, 1627–1632.

[40] S. Zhang, P. Kang, T. J. Meyer, *J. Am. Chem. Soc.* **2014**, *136*, 1734–1737.

[41] C. S. Cao, D. D. Ma, J. F. Gu, X. Y. Xie, G. Zeng, X. F. Li, S. G. Han, Q. L. Zhu, X. T. Wu, Q. Xu, *Angew. Chem. Int. Ed.* **2020**, *59*, 15014–15020.

[42] Y. Z. Li, J. L. Chen, S. Chen, X. L. Liao, T. T. Zhao, F. Y. Cheng, H. Wang, *ACS Energy Lett.* **2022**, *7*, 1454–1461.

[43] S. Chen, A. C. Chen, *J. Phys. Chem. C* **2019**, *123*, 23898–23906.

[44] Z. X. Yang, H. Z. Wang, X. Fei, W. H. Wang, Y. Z. Zhao, X. S. Wang, X. J. Tan, Q. S. Zhao, H. P. Wang, J. X. Zhu, L. Zhou, H. Ning, M. B. Wu, *Appl. Catal. B* **2021**, *298*, 9.
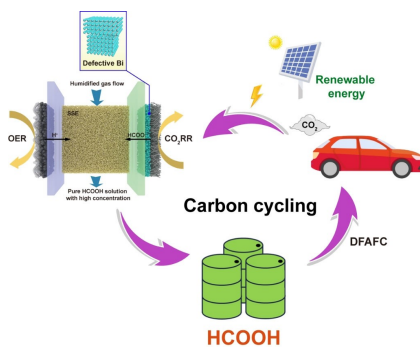
Research Articles

Research Articles

Electrochemical CO₂ reduction

C. Zhang, X. Hao, J. Wang, X. Ding,
Y. Zhong, Y. Jiang, M.-C. Wu, R. Long,
W. Gong, C. Liang, W. Cai,* J. Low,*
Y. Xiong* —————————— e202317628

Concentrated Formic Acid from CO₂ Electrolysis for Directly Driving Fuel Cell

The continuous production of pure formic acid solution with high concentration (2 M) for more than 300 h was achieved by using an MEA electrolyzer containing solid state electrolytes equipped with our developed moist heat ventilation collection system. The resultant formic acid could directly serve as the fuel for air-breathing formic acid fuel cells, which closed the carbon cycle loop of the formic acid economy.